

Regional gravity field modeling using free-positioned point masses

MIAO LIN, HEINER DENKER AND JÜRGEN MÜLLER

Institut für Erdmessung (IfE), Leibniz Universität Hannover, Hannover, Germany
(linmiao@ife.uni-hannover.de)

Received: July 23, 2013; Revised: November 5, 2013; Accepted: November 19, 2013

ABSTRACT

A two-step free-positioned point mass method is used for regional gravity field modeling together with the remove-compute-restore (RCR) technique. The Quasi-Newton algorithm (L-BFGS-B) is implemented to solve the nonlinear problem with bound constraints in the first step, while in the second step the magnitudes of the point masses are re-adjusted with known positions in the least-squares sense. In order to reach a good representation of the gravity field, a number of parameter sets have to be defined carefully before the computations. The effects of four important parameter sets (depth limits, number of point masses, original/reduced basis functions and optimization directions) are investigated for regional gravity field modeling based on two numerical test cases with synthetic and real data. The results show that the selection of the initial depth and depth limits is of most importance. The number of point masses for obtaining a good fit is affected by the data distribution, while a dependency on the data variability (signal variation) is negligible. Long-wavelength errors in the predicted height anomalies can be reduced significantly by using reduced basis functions, and the radial-direction optimization proves to be stable and reliable for regular and irregular data scenarios. If the parameter sets are defined properly, the solutions are similar to the ones computed by least-squares collocation (LSC), but require fewer unknowns than LSC.

Keywords: regional gravity field modeling, free-positioned point masses, depth limits

1. INTRODUCTION

In the field of geodesy, the determination of the external gravity field of the Earth is one of the main tasks. According to Newton's famous law, the potential exterior to the Earth's surface can be generated by infinitely many mass elements inside the Earth. However, it is impossible to know the exact mass distribution, and therefore a practicable way is to determine unobserved gravity field quantities based on observed ones, which may be considered as an inverse problem according to *Lehmann (1993)* and *Claessens et al. (2001)*. The available observations are always finite in practice, and as different mass configurations can generate the same gravity field, the non-uniqueness of the inverse problem is inevitable. Therefore, it is necessary to make some assumptions about the

gravity field to simplify the mathematical or physical model, e.g., by representing the gravity field by the sum of a finite number of spherical radial basis functions.

Recent global geopotential models (e.g., *Lemoine et al., 1998; Pavlis et al., 2012*) are commonly represented by spherical harmonics up to a certain degree of detail and resolution, but they don't have any localizing properties in the space domain and require global and homogeneous input data. Therefore, they are less suitable for regional gravity field modeling, in particular in the case of heterogeneous data (e.g., *Schmidt et al., 2007; Eicker, 2008; Bentel et al., 2013*). Alternately, numerical integration methods and least-squares collocation (LSC) together with the remove-compute-restore (RCR) technique are the standard methods for regional gravity field modeling (e.g., *Arabelos and Tscherning, 1988; Wang et al., 2012; Denker, 2013*). Another interesting approach is the parameter estimation method based on radial basis functions that decrease rapidly with the distance from their origins. This method is more flexible than the numerical integration method and requires fewer unknowns to be estimated in comparison to LSC (e.g., *Tscherning, 1981*). In recent years, various kinds of radial basis functions have been investigated for gravity field modeling (e.g., *Marchenko et al., 2001; Schmidt et al., 2007; Eicker, 2008; Klees et al., 2008; Tenzer and Klees, 2008; Wittwer, 2009; Bentel et al., 2013*). The point mass method, which is used in this paper, is one of these methods with simple basis functions. Obviously, the assembly of the point masses plays a crucial role in the modeling. There are two approaches to deal with this issue. The first option is the fixed-positioned approach, where a certain number of point masses with known positions inside the Earth are used to represent the gravity field. Usually these point masses are located at grid points at a constant depth (i.e., single-layer) or at various depths (i.e., multi-layer). The advantage of this approach is that only magnitudes of the point masses have to be estimated by solving a linear least-squares problem. The solution will become unstable in the case of data gaps as the point masses in the gaps will give similar columns in the design matrix of the linear system, and therefore a regularization is required. Moreover, the inhomogeneous data distribution is not fully taken into account in this approach, as the spacing and depths of the point masses are the same within a layer; some related studies can be found in *Reilly and Herbrechtsmeier (1978), Vermeer (1995), Ihde et al., (1998)* and *Chen (2006)*. The second option is the free-positioned approach in which the point masses are searched stepwise in connection with a simultaneous determination of their positions and magnitudes within an iterative least-squares approach. When the searching terminates, the number of point masses is known, and so are the positions. This approach is more flexible than the first approach, as the data variability and distribution can be considered during the searching process, but it is also much more complex; some examples can be found in *Barthelmes (1986, 1989), Lehmann (1993) and Claessens et al., (2001)*.

In order to reach a good representation of the regional gravity field by free-positioned point masses, a number of parameter sets need to be defined carefully. In this paper, a two-step free-positioned point mass method is proposed, in which a Quasi-Newton algorithm L-BFGS-B (e.g., *Zhu et al., 1994; Byrd et al., 1995*) is implemented to solve the nonlinear problem with bound constraints. The main goal is to investigate the effects of four important parameter sets (i.e., depth limits, number of point masses, original/reduced basis functions and optimization directions) for regional gravity field modeling, and to derive appropriate parameter setups for different scenarios. Section 2 gives a brief

description of the method, the L-BFGS-B algorithm, and the relevant parameter sets. Two numerical test cases with synthetic and real data are described in Section 3, and numerical results from the point mass method and corresponding least-squares collocation solutions are discussed in Section 4. Finally, Section 5 gives some conclusions drawn from the results.

2. METHOD

In this paper, the free-positioned point mass method is implemented as a two-step approach, where the first step deals with the searching and optimization of the point mass positions. Then in the second step, the point mass positions are held fixed and the magnitudes are readjusted by solving a linear least-squares problem, where Tikhonov regularization (Tikhonov, 1963; Bouman, 1998; Hansen, 2008) may be introduced to solve the ill-posedness caused by large point mass depths, masses located in close proximity, or data gaps.

2.1. Mathematical formulation

The disturbing potential exterior to the Earth's surface can be represented by a set of N point masses as

$$T_i = \sum_{j=1}^N \mu_j \phi_{ij} (r_i, \varphi_i, \lambda_i, r_j, \varphi_j, \lambda_j), \quad (1)$$

where μ_j is the magnitude of the j -th point mass; r , φ and λ stand for the radial distance, geocentric latitude and longitude, respectively, and ϕ_{ij} is the point mass basis function which is given as

$$\phi_{ij} = \frac{1}{l_{ij}}, \quad (2a)$$

where $l_{ij} = \sqrt{r_i^2 + r_j^2 - 2r_i r_j \cos \psi_{ij}}$ denotes the distance between the i -th computation point and the j -th point mass, and ψ_{ij} is the corresponding spherical distance defined as

$$\cos \psi_{ij} = \sin \varphi_i \sin \varphi_j + \cos \varphi_i \cos \varphi_j \cos (\lambda_i - \lambda_j). \quad (2b)$$

If the point mass positions are known, the magnitudes can be estimated by solving a linear least-squares problem. On the contrary, if the positions are left free, the unknown model parameters also include the positions and not just the magnitudes, which leads to a nonlinear least-squares problem. In this case, the set of model parameters for N point masses can be expressed as

$$\mathbf{m} = (\mu_1, r_1, \varphi_1, \lambda_1, \dots, \mu_N, r_N, \varphi_N, \lambda_N)^T. \quad (3)$$

The corresponding objective function to be minimized is given as

$$\Psi(\mathbf{m}) = (\mathbf{d}_{\text{obs}} - \mathbf{F}(\mathbf{m}))^T \mathbf{P}(\mathbf{d}_{\text{obs}} - \mathbf{F}(\mathbf{m})), \quad (4)$$

where \mathbf{d}_{obs} is the data vector, \mathbf{F} is the operator vector, $\mathbf{F}(\mathbf{m})$ can be expressed by Eq. (1) or corresponding derivatives, depending on the data types, and \mathbf{P} denotes the weight matrix of the observations. In this paper, the observations are assumed to have the same accuracy, and hence \mathbf{P} is an identity matrix.

In order to minimize the objective function in Eq. (4), an iterative procedure is implemented to estimate the vector of model parameters \mathbf{m} by the following equation

$$\mathbf{H}(\mathbf{m}_k)(\Delta\mathbf{m}_k) = -\mathbf{g}(\mathbf{m}_k), \quad (5)$$

where $\Delta\mathbf{m}_k = \mathbf{m}_{k+1} - \mathbf{m}_k$ is the perturbation vector of the k -th iteration. The related gradient and Hessian of the objective function are denoted as $\mathbf{g}(\mathbf{m}_k)$ and $\mathbf{H}(\mathbf{m}_k)$, and can be expressed as

$$\mathbf{g}(\mathbf{m}_k) = \left. \frac{\partial \Psi(\mathbf{m})}{\partial \mathbf{m}} \right|_{\mathbf{m}=\mathbf{m}_k}, \quad \mathbf{H}(\mathbf{m}_k) = \left. \frac{\partial^2 \Psi(\mathbf{m})}{\partial \mathbf{m}^2} \right|_{\mathbf{m}=\mathbf{m}_k}. \quad (6)$$

In the light of Eqs (5) and (6), the gradient and Hessian are required to estimate the perturbation vector in the iterative process. In this paper, the Quasi-Newton algorithm L-BFGS-B is introduced to solve the nonlinear problem iteratively. It is an extension of the L-BFGS algorithm (Liu and Nocedal, 1989; Nocedal and Wright, 1999), and minimizes the objective function with simple bounds for the model parameters

$$\Psi(\mathbf{m}) = (\mathbf{d}_{\text{obs}} - \mathbf{F}(\mathbf{m}))^T \mathbf{P}(\mathbf{d}_{\text{obs}} - \mathbf{F}(\mathbf{m})), \quad \text{subject to } \mathbf{m}_{\min} \leq \mathbf{m} \leq \mathbf{m}_{\max}, \quad (7)$$

where \mathbf{m}_{\min} and \mathbf{m}_{\max} are the lower and upper bounds for the model parameters. The L-BFGS-B algorithm allows to approximate the non-diagonal inverse Hessian $\mathbf{B}(\mathbf{m}_k)$ from the last ℓ gradient- and model-difference vectors (usually, $3 \leq \ell \leq 7$), which is generally updated in the iteration through the following formula

$$\mathbf{B}(\mathbf{m}_{k+1}) = \mathbf{V}_k^T \mathbf{B}_k \mathbf{V}_k + \gamma_k \mathbf{p}_k \mathbf{p}_k^T, \quad (8)$$

where $\mathbf{p}_k = \mathbf{m}_{k+1} - \mathbf{m}_k$, $\mathbf{q}_k = \mathbf{g}(\mathbf{m}_{k+1}) - \mathbf{g}(\mathbf{m}_k)$, $\gamma_k = 1 / \left(\mathbf{q}_k^T \mathbf{p}_k \right)$, $\mathbf{V}_k = \mathbf{I} - \gamma_k \mathbf{q}_k \mathbf{p}_k^T$, and \mathbf{I} is the identity matrix. Consequently, the solution of the linear system in Eq. (5) and a regularization for solving the ill-posedness in Eq. (5) are avoided, and the perturbation vector can be obtained directly from

$$\Delta\mathbf{m}_k = -\mathbf{B}(\mathbf{m}_k) \mathbf{g}(\mathbf{m}_k). \quad (9)$$

Finally, the model parameters are updated as follows

$$\mathbf{m}_{k+1} = \mathbf{m}_k + \alpha \Delta\mathbf{m}_k, \quad (10)$$

where α is the step width that is determined by a line search procedure. It enables the objective function at the current iteration to be smaller than the one at the previous iteration. For more details about the L-BFGS and L-BFGS-B algorithms, one may refer to

Byrd et al. (1995) and Nocedal and Wright (1999); furthermore, some useful applications of the algorithms in geophysics and hydraulic engineering can be found in Guitton and Symes (2003), Ding et al. (2004), Brossier et al. (2009) and Asnaashari et al. (2013).

In order to save computing time, the first step of the free-positioned point mass method based on the L-BFGS-B algorithm is implemented as follows (e.g., Barthelmes 1986, 1989; Lehmann, 1993; Claessens et al., 2001):

Task 1: Choose the initial position for the first point mass at a proper depth D_0^1 under the data point with the maximum absolute value. Set the initial model parameter vector of the first point mass $\mathbf{m}_0^1 = (\mu_0^1, r_0^1, \phi_0^1, \lambda_0^1)^T$, where the superscript is the index for the point mass (1 in the case of the first point mass) and the subscript is the iteration number (0 means the initial values). Then determine the refined parameter vector for the first point mass $\mathbf{m}_n^1 = (\mu_n^1, r_n^1, \phi_n^1, \lambda_n^1)^T$ by the L-BFGS-B algorithm using n iterations.

Tasks 2 to N_ϵ : Choose the initial position for the second point mass in the same way as above, which means under the data point with the maximum absolute difference between the given and modeled value based on Task 1; then improve the model parameters for the second point mass by the L-BFGS-B algorithm based on the corresponding initial model parameters. Set the existing model parameters associated with all point masses chosen so far (2 for task number 2) as the initial parameter vector and use the L-BFGS-B algorithm again to derive iteratively the refined parameter vector. Continue this procedure until N_ϵ mass points are jointly determined.

Tasks $N_\epsilon + 1$ to N : Continue the determination of further mass points until the final number N is reached, but in order to save computation time and make the entire problem manageable, readjust by the L-BFGS-B algorithm only the actually processed point mass together with the N_ϵ point masses located closest to it, while keeping the remaining point mass parameters fixed.

The total number of mass points N is determined usually by specifying a limit for the data misfit or just by defining the maximum number of the point masses. The latter option is used in this paper.

After the first step within the entire procedure is completed, the second step is conducted, which is to improve in the least-squares sense the magnitudes of all selected point masses based on known positions by minimizing the objective function

$$\Psi(\mathbf{x}) = (\mathbf{Ax} - \mathbf{d}_{\text{obs}})^T \mathbf{P}(\mathbf{Ax} - \mathbf{d}_{\text{obs}}), \quad (11)$$

where \mathbf{x} is the vector of the magnitudes, and \mathbf{A} is the design matrix in which the elements are defined by Eq. (2a) or corresponding derivatives. Suppose that A_{ij} is one element of \mathbf{A} , and the observations are gravity anomalies, then A_{ij} is given by

$$A_{ij} = \left(-\frac{\partial}{\partial r_i} - \frac{2}{r_i} \right) \frac{1}{l_{ij}} = \frac{r_i - r_j \cos \psi_{ij}}{l_{ij}^3} - \frac{2}{r_i l_{ij}} = \sum_{n=0}^{\infty} (n-1) \frac{1}{r_i^2} \left(\frac{r_j}{r_i} \right)^n P_n(\cos \psi_{ij}), \quad (12)$$

and the corresponding element A_{ij}^r for the reduced basis function (excluding the terms $0 - n_{max}$) is defined as

$$A_{ij}^r = \sum_{n=n_{max}+1}^{\infty} (n-1) \frac{1}{r_i^2} \left(\frac{r_j}{r_i} \right)^n P_n(\cos \psi_{ij}) = A_{ij} - \sum_{n=0}^{n_{max}} (n-1) \frac{1}{r_i^2} \left(\frac{r_j}{r_i} \right)^n P_n(\cos \psi_{ij}). \quad (13)$$

The notations in the above two equations are the same as the ones in Eqs (1) and (2a), and P_n are the Legendre polynomials.

As the positions of the point masses, resulting from the first (iterative) step, may be located close together in some cases, numerical instabilities may occur in the adjustment process within the second step. Therefore, the Tikhonov regularization is introduced to stabilize the solution, and the objective function is then given by

$$\Psi(\mathbf{x}) = (\mathbf{Ax} - \mathbf{d}_{obs})^T \mathbf{P}(\mathbf{Ax} - \mathbf{d}_{obs}) + \lambda \mathbf{x}^T \mathbf{Kx}, \quad (14)$$

where the first term of the right-hand side is associated with the data misfit between the predictions and observations, and the second term is the regularization term with the positive definite (regularization) matrix \mathbf{K} , which is defined as an identity matrix in this paper, and the regularization parameter λ balances the contributions between both terms. The solution of Eq. (14) with $\mathbf{P} = \mathbf{K} = \mathbf{I}$ becomes

$$\mathbf{x}_\lambda = \left(\mathbf{A}^T \mathbf{A} + \lambda \mathbf{I} \right)^{-1} \mathbf{A}^T \mathbf{d}_{obs}. \quad (15)$$

2.2. Relevant parameter sets

A number of parameter sets need to be defined appropriately before starting the computations. Four different parameter sets will be discussed in this paper.

1. The initial depth and depth limits for the point masses: As the observations in connection with the RCR technique are residuals, where long-wavelength components from a global geopotential model are removed, the point masses should not be located too deep. The deeper the point masses are, the less orthogonal the basis functions become (e.g., *Claessens et al., 2001*). On the other hand, the masses should not be too shallow either to avoid overparameterization and extremely local features. As the depths of the point masses are one of the key factors for the performance of the computed model, it is important to introduce appropriate depth constraints to the nonlinear problem. For this purpose, the L-BFGS-B algorithm is a suitable choice as it can handle the nonlinear problem with bound constraints. The initial depths may be chosen based on the data spacing or the correlation length of the empirical covariance function derived from the observations, so are the depth limits.
2. The number of point masses: The number of point masses is dependent on the data variability and distribution as well as the targeted level for the data misfit. More

point masses are required in an area with rugged signals, while fewer masses can be used to represent smooth signals. Furthermore, the addition of each new point mass may decrease the data misfit, but it also reduces the redundancy.

3. The original/reduced point mass basis functions: Long-wavelength errors will be introduced into the solutions by using original basis functions due to the different spectral bands associated with the residual observations and the basis functions. The use of reduced basis functions may give better height anomaly solutions, which are sensitive to long-wavelength signals. The solutions computed by two kinds of basis functions will be compared in the following numerical test cases. Noting that a lot of computation time is needed for the reduced basis functions in the first step without obtaining significantly improved results, the reduced basis functions are only employed in the second step of this approach.
4. The optimization directions: Besides the magnitude of each new point mass, the positions can be optimized in all directions or only in radial direction. Regarding the optimization in all directions, usually some point masses tend to move into the gaps, while minimizing the data misfit, and if the upper depth limit is too shallow, the estimated magnitudes for these masses may become too large and lead to unreasonable small-scale local signals. In addition, the all-direction optimization may relocate masses near the edge of the data area far away from the initial locations, resulting in serious numerical instabilities. Hence, additional horizontal constraints must be added. Such circumstances can be avoided by using only the radial-direction optimization.

More details on further possible parameter sets can be found in *Claessens et al. (2001)*. In this paper, the same initial depths and depth limits are used for each new point mass, the number of iterations for each added point mass is limited (e.g., 20), and only a small number of point masses (e.g., 10) around the new point mass are readjusted together with the new one.

3. NUMERICAL TESTS

Two numerical test cases with synthetic and real data are conducted to investigate the effects of the above mentioned four parameter sets in regional gravity field modeling. The solutions computed by the original and reduced basis functions are denoted as ‘S1’ and ‘S2’ and the ones corresponding to the all-direction and radial-direction optimization are denoted as ‘4P’ and ‘2P’ in the following. Consequently, e.g., the notation ‘S1+2P’ indicates that the solution is computed by using the original basis functions and a radial-direction optimization.

3.1. Data sets

The first (synthetic) data set contains 4753 regular gravity observations which are simulated from the Earth Gravity Model 2008 (EGM08 model, *Pavlis et al., 2012*) from degree 361 up to 2160. The research area is chosen to be the central Alps with an extension of 7°–15°E and 45°–49°N. The height for each observation is derived from the DTM2006.0 terrain model (*Pavlis et al., 2007*), and all observations are assumed to be error-free. The statistics of this data set is: *mean* = –0.486 mGal; root mean square

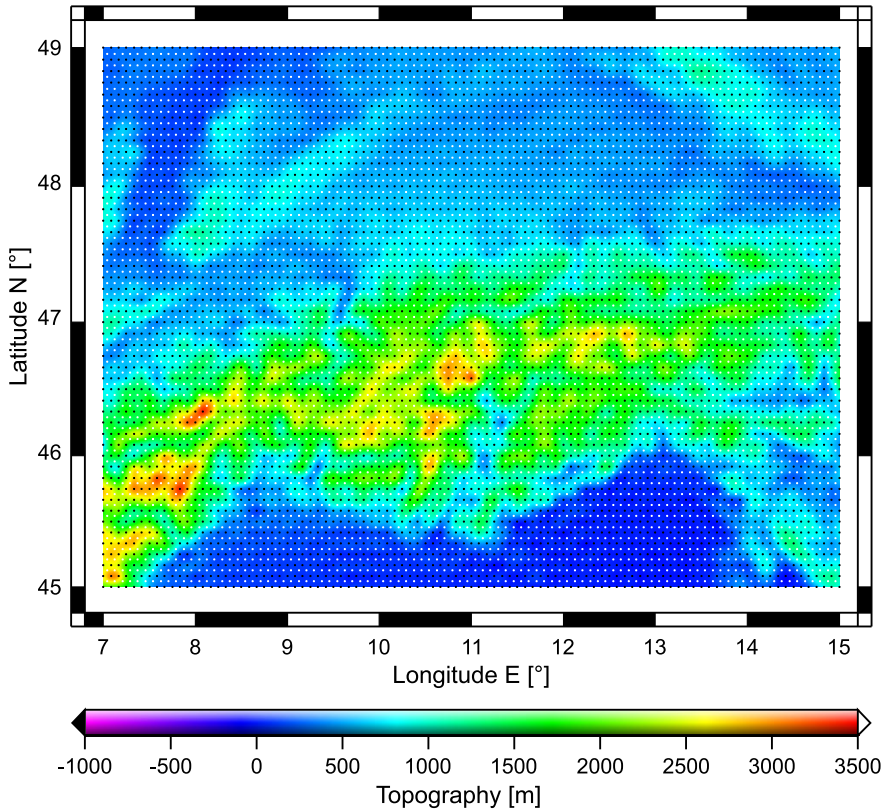


Fig. 1. Locations of gravity observations (black dots) and control points (white dots) for the synthetic test case; the background shows the topography of the research area derived from the DTM2006.0 terrain model.

$RMS = 16.809$ mGal; $min = -99.128$ mGal and $max = +62.917$ mGal. In addition, 4608 independent control points with true values, located half-way between the observations, are used to assess the quality of the predicted gravity and height anomalies. The locations of all points and the topography of the research area are illustrated in Fig. 1.

The second data set consists of 2767 real gravity measurements that are located in the area of New Mexico, USA, with an extent of -108° to $-105^\circ E$ and 31.5° to $35^\circ N$. The accuracy of the observations is about 2 mGal (Kearsley et al., 1985) and the associated statistics is: $mean = -0.453$ mGal; $RMS = 12.808$ mGal; $min = -40.724$ mGal and $max = +42.622$ mGal. Furthermore, 153 independent gravity measurements and 20 GPS/leveling stations are used as control points. Fig. 2 shows the locations of all points. According to the RCR technique, residuals are used for the modeling and further validation, where long-wavelength contributions from the EGM08 model complete to degree 360 and short-wavelength signals based on the RTM approach (Forsberg, 1984) are removed.

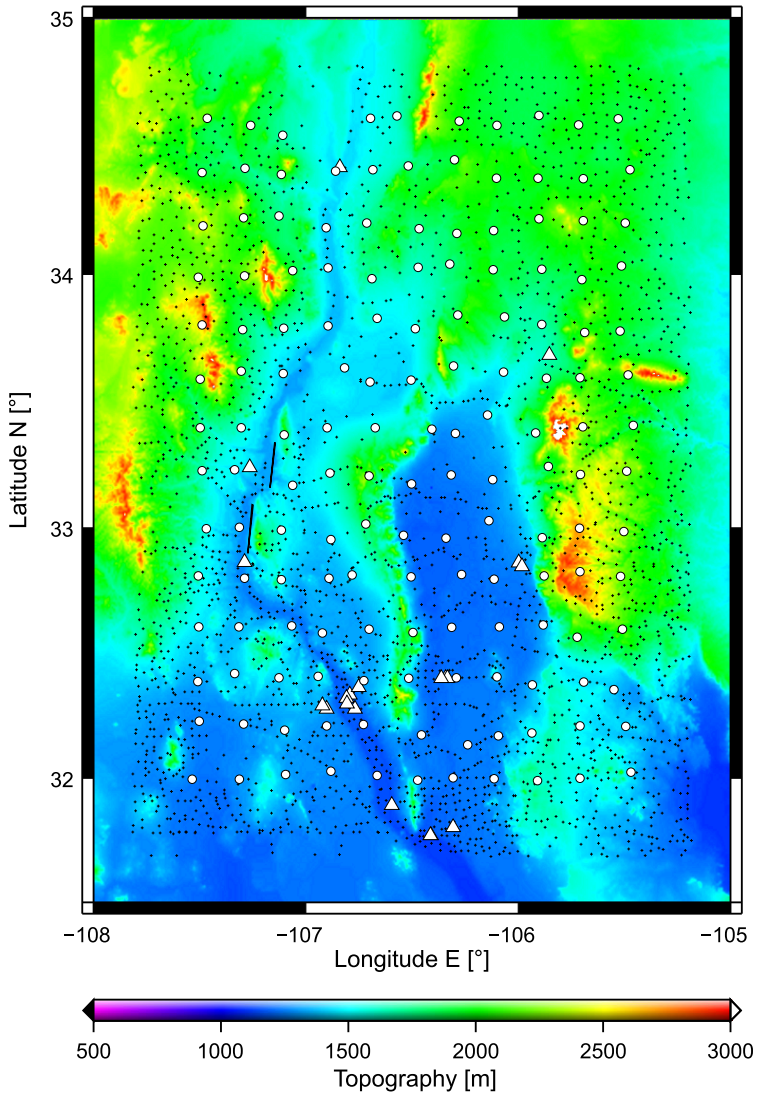


Fig. 2. Locations of 2767 gravity measurements (black dots), 153 gravity control points (white circles), and 20 GPS/leveling stations (white triangles) for the New Mexico test case; the background shows the topography of the research area.

3.2. Parameter setups

Several scenarios are considered to study the sensitivity of the gravity field solutions with respect to the aforementioned four parameter sets. As shown in *Hauck and Lelgemann (1985)*, the Krarup reproducing kernel defines the potential of a point mass

located below the observation point at a depth given by the Kelvin transformation at the Bjerhammar sphere, and if the number of mass points equals the number of observations, the point mass method can be considered as being equivalent to least-squares collocation with a covariance function defined by the Krarup kernel (*Barthelmes, 1989*). In regional gravity field modeling by collocation, the covariance function is always chosen to fit the empirical covariance function of the observations. Therefore, it seems to be quite reasonable to choose the initial depth of the point masses with the help of the empirical covariance function. The idea is to set the initial depth equal to the depth of the points mass basis function for which the corresponding half width ξ (i.e., where the function attains half of its maximum value) and the correlation length ξ_e of the empirical covariance function match. Once ξ_e is known, it is easy to derive the initial depth iteratively.

The empirical and analytical covariance functions for the two test cases are shown in Fig. 3, the latter ones being used with LSC. As a result, the correlation lengths are 0.108° and 0.101° for the synthetic and New Mexico data sets, and the corresponding estimates for the initial depths are about 15 and 13 km, respectively. Furthermore, the effects of four different sets of depth limits will be studied for each test area. The lower depth limits for the first three cases (see Table 1) are based on the simple formula $D = R/(n-1)$ given in *Bowin (1983)*, where D means the depth, R denotes a mean Earth radius, and n stands for the spherical harmonic degree; based on the maximum degree of the chosen reference field ($n = 360$), this results in a lower depth limit of about 20 km. In addition to this, also a deeper limit is chosen for each test area to study the corresponding impact on the results (see Case 4 in Table 1). Regarding the upper depth limit, practical investigations showed that this value should not be smaller than the average data spacing, as otherwise strong local unrealistic (erratic) features will show up; based on these considerations, the upper depth limits are chosen to be equal to or larger than the average data spacing. Nevertheless, a smaller upper depth limit is also selected for each test area for comparison

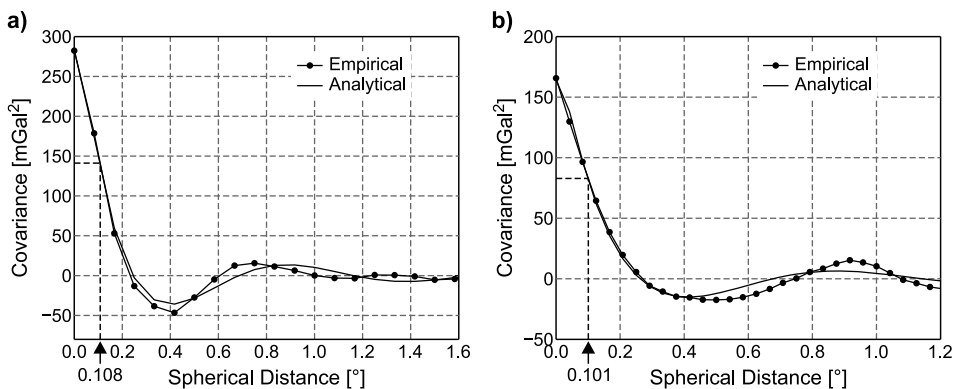


Fig. 3. Empirical and analytical covariance functions of the observations for **a)** the synthetic and **b)** the New Mexico test case. The corresponding correlation lengths of the empirical covariance functions are 0.108° and 0.101° .

Table 1. Parameter sets used in the numerical test cases.

Parameter Sets	Synthetic Test Case		New Mexico Test Case	
Basis functions	1	Original ('S1')	1	Original ('S1')
	2	No 0–200 terms ('S2')	2	No 0–100 terms ('S2')
Optimization directions	1	Radial-direction ('2P')	1	Radial-direction ('2P')
	2	All-direction ('4P')	2	All-direction ('4P')
Initial depth [km]	15		13	
Depth limits [km]	1	5–20	1	3–20
	2	9–20	2	6–20
	3	13–20	3	11–20
	4	13–50	4	11–30
Horizontal limits for '4P'	7.0°–15.0°E 45.0°–49.0°N		–107.85°– –105.15°E 31.65°–34.85°N	
N_{\in}	10		10	
Number of point masses	1	1100	1	700
	2	1500	2	1000
Iterations for each added point mass	20		20	
Regularization in the second step?	No		Yes	

purposes (see Case 1 in Table 1). With respect to the reduced basis functions, two cases are used in the synthetic and New Mexico test areas, where the terms from $n = 0$ –200 and $n = 0$ –100 are set to zero. All different parameter sets are summarized in Table 1. No regularization is used in the second step for the synthetic test area, but Tikhonov regularization is employed for the New Mexico test area, where the regularization parameter λ is determined by minimizing the *RMS* of the differences between predicted and observed gravity values on 153 control points. A similar approach can be found in *Tenzer and Klees (2008)* to determine the optimal depths of the basis functions for local gravity field modeling. For further details on the choice of the regularization parameter, we refer to *Bouman (1998)* and *Hansen (2008)*.

4. RESULTS AND DISCUSSION

The main results based on two different total numbers of point masses N are shown in Figs 4 and 5 for the synthetic test case, while corresponding results for the New Mexico test case are displayed in Figs 6 and 7. The figures show the statistics (root mean square *RMS*, standard deviation *STD*, and *range*) of the differences between predicted and observed values at the control points for the different parameter setups listed in Table 1. Figs 8 and 9 show the *RMS* of the differences between the predictions and observations (data misfit) as well as the *RMS* of the differences between predicted and observed values at the gravity control points (*RMS* difference) for different maximum numbers of point masses; both figures are based on the reduced point mass basis functions, and similar results are obtained when using the original basis functions (not shown here).

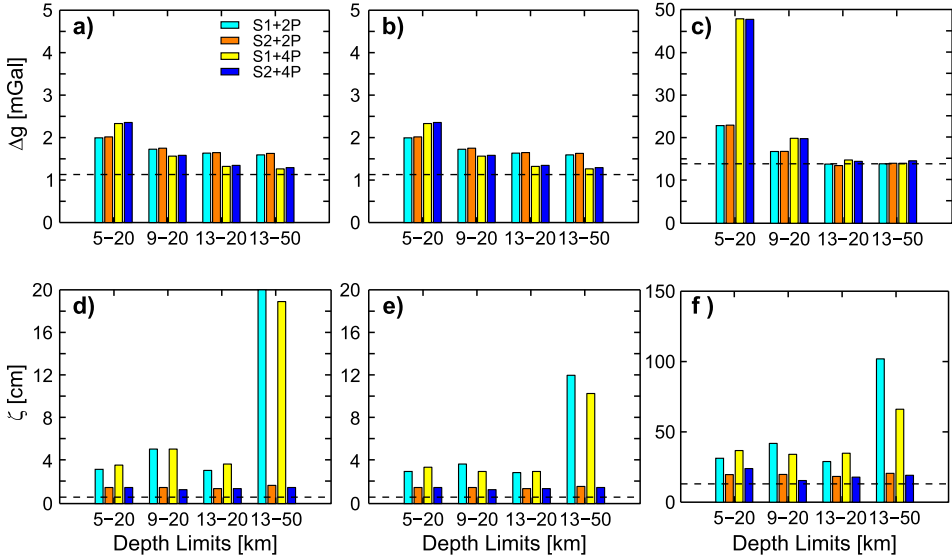


Fig. 4. Synthetic test case: **a)** root mean squares (*RMS*), **b)** standard deviations (*STD*) and **c)** *range* of the differences between predicted and true values for gravity anomalies (Δg) at control points associated with different parameter setups; **d)**, **e)** and **f)** the same for height anomalies (ζ). 1100 point masses are selected for the modeling, and the related least-squares collocation results are shown as dashed lines.

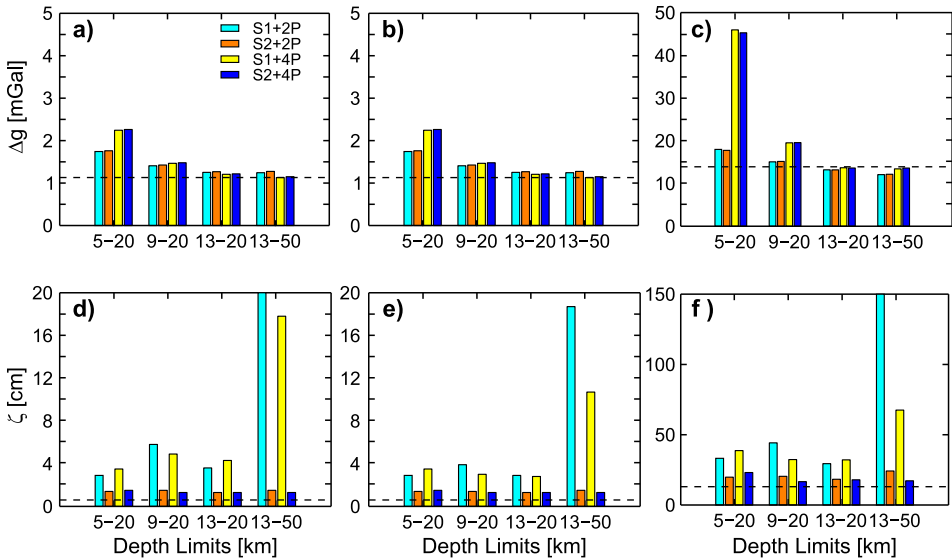


Fig. 5. The same as in Fig. 4, but for 1500 point masses selected for the modeling.

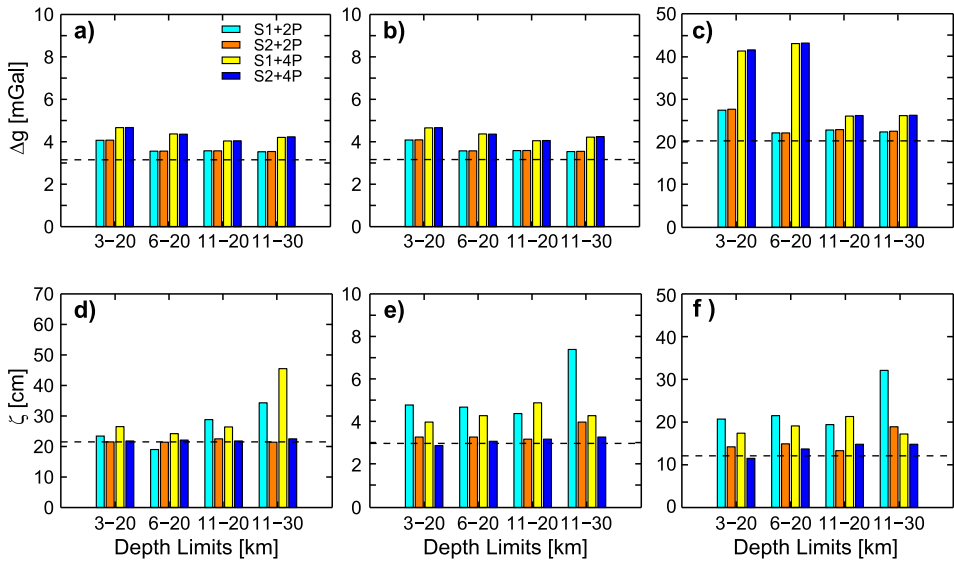


Fig. 6. The same as in Fig. 4, but for the New Mexico test case. 700 point masses are selected for the modeling.

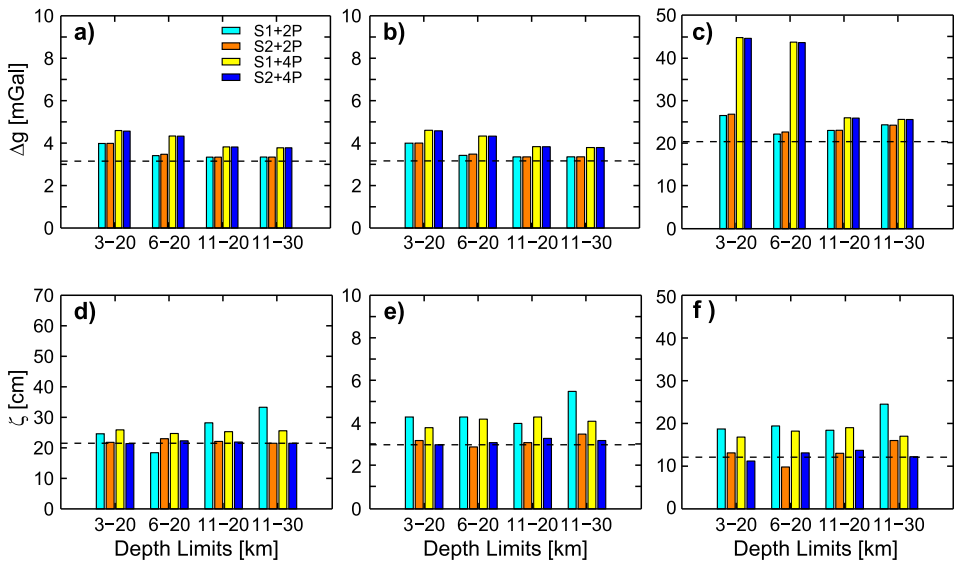


Fig. 7. The same as in Fig. 6, but for 1000 point masses selected for the modeling.

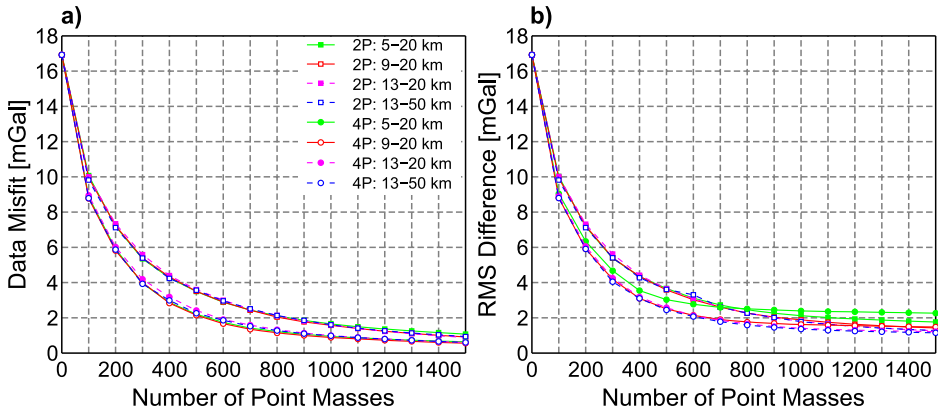


Fig. 8. Synthetic test case: **a)** data misfit and **b)** *RMS* difference at 4608 gravity control points with respect to different numbers of selected point masses associated with different depth limits and optimization directions. All results are computed by using the reduced point mass basis functions.

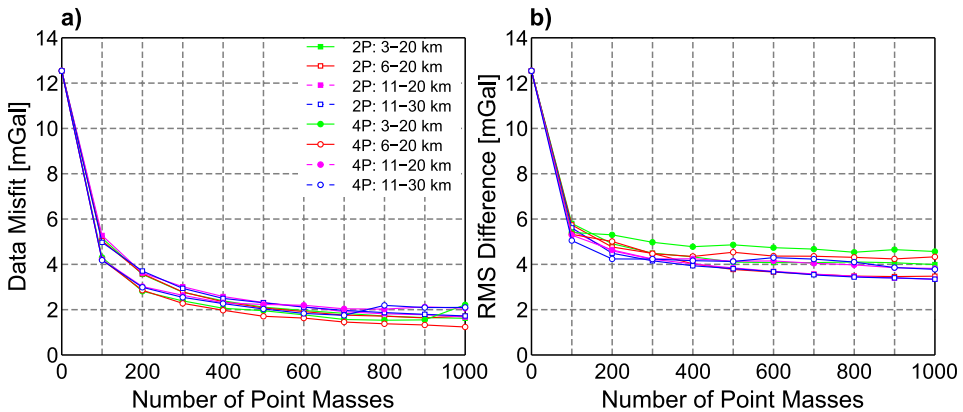


Fig. 9. The same as in Fig. 8, but for the New Mexico test case and 153 gravity control points in **b)**.

In addition to this, Table 2 gives the statistics of the differences between predicted values from the free-positioned point mass method as well as least-squares collocation and the true (simulated) values at the control points for the synthetic test area, while Table 3 includes corresponding results for the New Mexico test area based on 153 observed gravity anomaly and 20 height anomaly (GPS/leveling) control points. The main findings are summarized in the following subsections.

4.1. The effect of the depth limits on the solutions

From Figs 4–7 (see the bar charts for different depth limits) it is obvious that a proper choice of the depth limits is crucial to guarantee a high-quality solution with small errors

in comparison with the control point values. Comparing the solutions with the same lower depth limits but different upper depth limits (i.e., the first three cases of the depth limits in Table 1), it can be seen that the gravity solutions are quite bad for a too shallow upper depth limit (i.e., 5 and 3 km for the synthetic and New Mexico test areas), resulting in large *RMS*, *STD* and *range* of the differences. This can be attributed to the point masses located at or close to the upper depth limit, which produce some artificial high-frequency signals in the voids between the masses, as the so-called bandwidths (e.g., Klees *et al.*, 2008; Wittwer, 2009) of these point masses are too small. When the upper depth limit is deeper (i.e., 9 and 13 km for the synthetic test case; 6 and 11 km for the New Mexico test case), the gravity solutions become much better with smaller errors when comparing with the values at the control points. No evident differences can be found between the height anomaly solutions associated with three different upper depth limits; since the height anomalies are quite insensitive to short-wavelength signals, the change of the upper depth limit has only minor effects. Now, for constant upper depth limits but different lower depth limits (depth limit Cases 3 and 4 in Table 1), contrary to the previous investigation, the gravity solutions are nearly unaffected by the different lower depth limits, but the predicted height anomalies are distorted by some deep-lying masses due to the high sensitivity with respect to long-wavelength signals. According to the above comparisons, the quality of gravity solutions is sensitive to the chosen upper depth limit, while the height anomaly solutions are mostly affected by the lower depth limit. Therefore, the depth limits must be chosen carefully based on the observations to be fitted, requiring shallower point masses for fitting high-frequency gravity signals and deeper masses for the long-wavelength height anomalies. The solutions related to the upper depth limits of 13 km for the synthetic test case and 11 km for the New Mexico test case are quite good and close to the corresponding LSC results. As a result, an upper depth limit of about 85% of the initial depth, derived according to the approach described in Section 3.2, is a reasonable choice. The lower depth limits obtained from the simple formula given in Bowin (1983) prove to be appropriate (e.g., 20 km) in our test cases, but deeper limits are also suitable (e.g., 50 and 30 km). No explicit rules can be given for the optimal choice of the depth limits. Usually, the selected upper depth limit is not expected to be smaller than the average data spacing (i.e., 9 and 6 km for the synthetic and New Mexico test areas, respectively), while the lower depth limit is preferred to be smaller than the maximum resolution of the chosen reference field (i.e., about 55 km for both test cases).

4.2. The effect of the number of point masses on the solutions

Comparing Figs 4 and 5 (i.e., 1100 and 1500 point masses for the synthetic test area) as well as Figs 6 and 7 (i.e., 700 and 1000 point masses for the New Mexico test area), the gravity solutions are improved obviously when more point masses are used, but improvements for the height anomalies are not evident. From Figs 8 and 9, the data misfit and *RMS* differences decrease rapidly at the beginning, but only very slowly when more and more point masses are included. If the number of point masses is about 30–35% of the number of the observations (i.e., 1500 versus 4753 for the synthetic test area, 1000 versus 2767 for the New Mexico test area), the obtained solutions are close to the corresponding LSC results. However, the number of point masses may also depend on the

Table 2. Statistics of the differences between predicted values from the free-positioned point mass method as well as least-squares collocation and the true (simulated) values at the control points for the synthetic test case, i.e. 4608 gravity anomaly (Δg) and 4608 height anomaly (ζ) control points, respectively. The depth limit is 13–50 km and the number of point masses is 1500 for the respective solutions.

Δg [mGal]	<i>Mean</i>	<i>STD</i>	<i>RMS</i>	<i>Min</i>	<i>Max</i>
LSC	−0.049	1.129	1.130	−8.830	5.078
S1+2P	−0.027	1.244	1.244	−7.243	4.827
S2+2P	−0.011	1.274	1.274	−6.944	5.212
S1+4P	−0.008	1.130	1.130	−4.903	8.519
S2+4P	−0.002	1.149	1.149	−5.054	8.560
ζ [cm]					
LSC	0.0	0.6	0.6	−5.3	7.7
S1+2P	40.3	18.7	44.4	−16.6	143.5
S2+2P	0.0	1.5	1.5	−12.0	12.2
S1+4P	14.2	10.7	17.8	−31.2	36.3
S2+4P	0.0	1.3	1.3	−7.7	9.5

Table 3. The same as in Table 2, but for the New Mexico test area with 153 Δg and 20 ζ (GPS/leveling) control points (observed). The depth limit is 11–20 km and the number of point masses is 1000 for the respective solutions.

Δg [mGal]	<i>Mean</i>	<i>STD</i>	<i>RMS</i>	<i>Min</i>	<i>Max</i>
LSC	0.025	3.161	3.151	−8.444	11.926
S1+2P	0.039	3.351	3.340	−9.826	13.174
S2+2P	0.013	3.351	3.340	−9.909	13.131
S1+4P	0.050	3.833	3.821	−10.546	15.415
S2+4P	0.030	3.830	3.818	−10.505	15.384
ζ [cm]					
LSC	21.3	3.0	21.5	15.5	27.6
S1+2P	27.9	4.0	28.2	18.4	36.8
S2+2P	21.8	3.1	22.1	14.1	27.1
S1+4P	25.0	4.3	25.3	15.8	34.8
S2+4P	21.6	3.3	21.9	14.1	27.8

signal variation; in general, high-frequency signals can be represented better by more and more point masses, but may also entail additional instability problems.

4.3. The effect of the original/reduced basis functions on the solutions

Significant differences between the ‘S1’ (i.e., original point mass basis functions) and ‘S2’ (i.e., reduced basis functions) gravity solutions are not evident in Figs 4–7 and Tables 2 and 3. However, for the height anomaly solutions, the situation is completely

different, with the 'S2' solutions being significantly improved compared to the 'S1' solutions. Since the observations are residual gravity anomalies in our test cases, long-wavelength errors caused by different spectral bands associated with the original basis functions and the observations are evident in the height anomaly solutions, resulting in significant biases. Therefore, the reduced basis functions are recommended for quasigeoid modeling when only gravity anomalies are used as input data. However, also the 'S2' height anomaly solutions are slightly worse than corresponding LSC solutions in our test areas, which may be due to edge effects caused by the limited data coverage. A simple way to reduce edge effects is to make the data area larger than the model area.

4.4. The effect of the optimization directions on the solutions

In the synthetic test area (see Figs 4, 5 and 8 as well as Table 2), the '4P' solutions (i.e. all-direction optimization) perform better than the corresponding '2P' solutions (i.e. radial-direction optimization) in approximating the gravity values (except for the case with depth limits of 5–20 km), while for the height anomaly approximation both approaches in connection with the reduced basis function give very similar results. Only the reduced basis functions are utilized here, as the original basis functions affect the height anomaly solutions significantly (see previous Section 4.3). Furthermore, the results indicate that the all-direction optimization (4P) is more sensitive to the chosen upper depth limit than the radial-direction optimization (2P).

Similar comparisons are conducted in the New Mexico test area (see Figs 6, 7 and 9 as well as Table 3). Regarding again the '4P' and '2P' cases, the corresponding height anomaly solutions perform very similar, but larger discrepancies can be seen in the '4P' gravity solutions within the data gaps. Consequently, the data gaps are a critical issue for the all-direction optimization (4P), while reliable results can be obtained with the radial-direction optimization (2P) for both test areas with regular and irregular data, respectively.

5. CONCLUSIONS

The effects of four parameter sets on regional gravity field modeling by the two-step free-positioned point mass method are investigated numerically in two different test areas with synthetic and real data. The L-BFGS-B algorithm is demonstrated to be suitable for solving the bound-constrained nonlinear least-squares problem in the first step of the entire procedure. However, the quality of the final solutions is highly dependent on the choice of four parameter sets, and although an improper choice may still lead to a satisfactory data misfit, large errors can be found in the final solutions when comparing them with independent data.

The numerical results lead to the following conclusions:

1. The determination of the initial depth and depths limits is of most importance; they must be chosen very carefully to avoid unreliable solutions. The testing of different initial depths and related depth limits leads to the following empirical rule: the initial depth is derived from the empirical covariance function of the observations, and the upper depth limit is chosen to be 0.8–0.9 times this value, while being larger than the average data spacing; the lower depth can be selected by the simple

formula given in *Bowin (1983)*, but it should be less than the maximum resolution of the chosen reference field.

2. To get a good fit to the data in the selected test cases, the data distribution has an impact on the necessary number of point masses, but the data variability plays only a minor role. An efficient way for choosing the number of point masses is to terminate the first step of the method by satisfying a defined data misfit.
3. The reduced basis functions are recommended for quasigeoid modeling when using gravity anomalies only, as long-wavelength errors can be reduced significantly in the corresponding solutions. The number of terms excluded from the reduced basis functions can be equal to or less than the maximum degree of the chosen reference field.
4. If the depth limits are appropriate, the all-direction optimization performs slightly better than the radial-direction optimization in the synthetic test case with error-free data. However, the all-direction option is very sensitive to the upper depth limit as well as the data distribution, and large errors occur in corresponding solutions for the real test case with data gaps. The radial direction option is more reliable and simple.
5. The *RMS* minimization approach works well for choosing the proper regularization parameter in the second step of the method for the New Mexico test case, but it is not very suitable for the case with a large number of observations or in the absence of control points. Therefore, some heuristic approaches for choosing the proper regularization parameter need to be incorporated in this method.

Acknowledgements: The first author was financially supported by the China Scholarship Council (CSC).

References

- Arabelos D. and Tscherning C.C., 1988. Gravity field mapping from satellite altimetry, sea-gravimetry and bathymetry in the Eastern Mediterranean. *Geophys. J. Int.*, **92**, 195–206.
- Asnaashari A., Brossier R., Garambois S., Audebert F., Thore P. and Virieux J., 2013. Regularized seismic full waveform inversion with prior model information. *Geophysics*, **78**, R25–R36.
- Barthelmes F., 1986. *Untersuchungen zur approximation des äußeren Schwerefeldes der Erde durch Punktmassen mit optimierten Positionen*. Report Nr. 92, Veröffentlichungen des Zentralinstitut Physik der Erde, Potsdam, Germany (in German).
- Barthelmes F., 1989. *Local Gravity Field Approximation by Point Masses with Optimized Positions*. Report Nr. 102(2). Veröffentlichungen des Zentralinstitut Physik der Erde, Potsdam, Germany.
- Bentel K., Schmidt M. and Gerlach C., 2013. Different radial basis functions and their applicability for regional gravity field representation on the sphere. *GEM-International Journal on Geomathematics*, **4**, 67–96.
- Bouman J., 1998. *Quality of Regularization Method*. DEOS Report Nr. 98.2, Delft Institute for Earth-Orient Space Research, Delft University of Technology, Delft, The Netherland.

- Bowin C., 1983. Depth of principal mass anomalies contributing to the Earth's geoidal undulations and gravity anomalies. *Mar. Geod.*, **7**, 61–100.
- Brossier R., Operto S. and Virieux J., 2009. Seismic imaging of complex onshore structures by 2D elastic frequency-domain full-waveform inversion. *Geophysics*, **74**, WCC105–WCC118.
- Byrd R.H., Lu P., Nocedal J. and Zhu C., 1995. A limited memory algorithm for bound constrained optimization. *SIAM J. Sci. Comput.*, **16**, 1190–1208.
- Chen W.Y., 2006. *A Study of Determination of Taiwan's Local Geoid by Combination of GPS Leveling and Gravity Data with Point Masses*. M.Sc. Thesis, National Cheng Kung University, Taiwan (in Chinese).
- Claessens S.J., Featherstone W.E. and Barthelmes F., 2001. Experiences with point-mass gravity field modeling in the Perth Region, Western Australia. *Geomatics Research Australasia*, **75**, 53–86.
- Denker H., 2013. Regional gravity field modeling: Theory and Practical Results. In: Xu G.C. (Ed.), *Science of Geodesy – II*. Springer Verlag, Heidelberg, Germany, 185–291.
- Ding Y., Jia Y.F. and Wang S.Y., 2004. Identification of Manning's roughness coefficients in shallow water flows. *J. Hydraul. Eng.-ASCE*, **130**, 501–510.
- Eicker A., 2008. *Gravity Field Refinement by Radial Basis Functions from In-Situ Satellite Data*. Ph.D. Thesis, University of Bonn, Bonn, Germany.
- Forsberg R., 1984. *A Study of Terrain Reductions, Density Anomalies and Geophysical Inversion Methods in Gravity Field Modeling*. Report 355, Department of Geodetic Science and Surveying, Ohio State University, Columbus, Ohio.
- Guittou A. and Symes W.W., 2003. Robust inversion of seismic data using the Huber norm. *Geophysics*, **68**, 1310–1319.
- Hansen P.C., 2008. *Regularization Tools. A Matlab Package for Analysis and Solution of Discrete Ill-Posed Problems - Version 4.1 for Matlab 7.3*. Informatics and Mathematical Modeling, Technical University of Denmark, Lyngby, Denmark (<http://www.imm.dtu.dk/~pch>).
- Hauck H. and Lelgemann D., 1985. Regional gravity field approximation with buried masses using least-norm collocation. *Manus. Geod.*, **10**, 50–58.
- Ilde J., Schirmer U., Stefani F. and Töppe F., 1998. Geoid modeling with point masses. *Proceedings of the Second Continental Workshop on the Geoid in Europe*, Budapest, Hungary, 199–204 (<https://www.hzdr.de/FWS/FWSH/Stefani/geoid.pdf>).
- Kearsley A.H.W., Sideris M.G., Krynski J., Forsberg R. and Schwarz K.P., 1985. *White Sands Revisited - A Comparison of Techniques to Predict Deflections of the Vertical*. Report No. 30007, Division of Surveying Engineering, University of Calgary, Alberta, Canada.
- Klees R., Tenzer R., Prutkin I. and Wittwer T., 2008. A data-driven approach to local gravity field modeling using spherical radial basis functions. *J. Geodesy*, **82**, 457–471.
- Lehmann R., 1993. The method of free-positioned point masses - geoid studies on the Gulf of Bothnia. *Bull. Geod.*, **67**, 31–40.

- Lemoine F.G., Kenyon S.C., Factor J.K., Trimmer R.G., Pavlis N.K., Chinn D.S., Cox C.M., Klosko S.M., Luthcke S.B., Torrence M.H., Wang Y.M., Williamson R.G., Pavlis E.C., Rapp R.H. and Olson T.R., 1998. *The Development of the Joint NASA GSFC and the National Imagery and Mapping Agency (NIMA) Geopotential Model EGM96*. NASA Technical Report TP-1998-206861, National Aeronautics and Space Administration, Goddard Space Flight Center, Greenbelt, MD, USA.
- Liu D.C. and Nocedal J., 1989. On the limited memory BFGS method for large scale optimization. *Math. Program.*, **45**, 503–528.
- Marchenko A.N., Barthelmes F., Mayer U. and Schwintzer P., 2001. *Regional Geoid Determination: An Application to Airborne Gravity Data in the Skagerrak*. Scientific Technical Report No. 01/07, GFZ, Potsdam, Germany (<http://gfzpublic.gfz-potsdam.de/pubman/item/escidoc:8522:3/component/escidoc:8521/0107.pdf>%3Bjsessionid=7BF9C98BB58B3B4EA8227BBFCF9C4FD8).
- Nocedal J. and Wright S.J., 1999. *Numerical Optimization*. Springer Series in Operations Research, Springer Verlag, New York.
- Pavlis N.K., Factor J.K. and Holmes S.A., 2007. Terrain-related gravimetric quantities computed for the next EGM. *Proceedings of the 1st International Symposium of the International Gravity Field Service "Gravity field of the Earth"*. *Harita Dergisi*, Special Issue 18, General Command of Mapping, Istanbul, Turkey, 318–323 (http://earth-info.nga.mil/GandG/wgs84/gravitymod/new_egm/EGM08_papers/NPavlis%26al_S8_Revised111606.pdf).
- Pavlis N.K., Holmes S.A., Kenyon S.C. and Factor J.K., 2012. The development and evaluation of the Earth Gravitational Model 2008 (EGM2008). *J. Geophys. Res.*, **117**, B04406, DOI: 10.1029/2011JB008916.
- Reilly J.P. and Herbrechtsmeier E.H., 1978. A systematic approach to modeling the geopotential with point mass anomalies. *J. Geophys. Res.*, **83**, 841–844.
- Schmidt M., Fengler M., Mayer-Guerr T., Eicker A., Kusche J., Sanchez L. and Han S., 2007. Regional gravity field modeling in terms of spherical base functions. *J. Geodesy*, **81**, 17–38.
- Tenzer R. and Klees R., 2008. The choice of the spherical radial basis functions in local gravity field modeling. *Stud. Geophys. Geod.*, **52**, 287–304.
- Tikhonov A.N., 1963. Solution of incorrectly formulated problems and the regularization method. *Soviet Math.*, **4**, 1035–1038.
- Tscherning C.C., 1981. Comparison of some methods for the detailed representation of the Earth's gravity field. *Rev. Geophys.*, **19**, 213–221.
- Vermeer M., 1995. Mass point geopotential modeling using fast spectral techniques: historical overview, toolbox description, numerical experiments. *Manus. Geod.*, **20**, 362–378.
- Wang Y.M., Saleh J., Li X. and Roman D.R., 2012. The US Gravimetric Geoid of 2009 (USGG2009): model development and evaluation. *J. Geodesy*, **86**, 165–180.
- Wittwer T., 2009. *Regional Gravity Field Modeling with Radial Basis Functions*. Ph.D. Thesis, Delft University of Technology, Delft, The Netherlands.
- Zhu C., Byrd R.H., Lu P. and Nocedal J., 1994. *LBFGS-B: Fortran Subroutines for Large-Scale Bound Constrained Optimization*. Report NAM-11, EECS Department, Northwestern University, Evanston, IL (www.ece.northwestern.edu/~nocedal/PSfiles/lbfgsb.ps.gz).